Since January 2020 Elsevier has created a COVID-19 resource centre with free information in English and Mandarin on the novel coronavirus COVID-19. The COVID-19 resource centre is hosted on Elsevier Connect, the company's public news and information website.

Biomedical Signal Processing and Control 77 (2022) 103860

Contents lists available at ScienceDirect

Biomedical Signal Processing and Control

journal homepage: www.elsevier.com/locate/bspc

CXGNet: A tri-phase chest X-ray image classification for COVID-19 diagnosis using deep CNN with enhanced grey-wolf optimizer

Anandbabu Gopatoti [a,b,*], P. Vijayalakshmi [a]

[a] Department of Electronics and Communication Engineering, Hindusthan College of Engineering and Technology, Coimbatore, Tamil Nadu, India
[b] Anna University, Chennai, Tamil Nadu, India

ARTICLE INFO

Keywords:
COVID-19
Chest X-ray image classification
Convolutional neural networks
Deep learning
Grey-wolf optimization

ABSTRACT

The coronavirus disease 2019 (COVID-19) epidemic had a significant impact on daily life in many nations and global public health. COVID's quick spread has become one of the biggest disruptive calamities in the world. In the fight against COVID-19, it's critical to keep a close eye on the initial stage of infection in patients. Furthermore, early COVID-19 discovery by precise diagnosis, especially in patients with no evident symptoms, may reduce the patient's death rate and can stop the spread of COVID-19. When compared to CT images, chest X-ray (CXR) images are now widely employed for COVID-19 diagnosis since CXR images contain more robust features of the lung. Furthermore, radiologists can easily diagnose CXR images because of its operating speed and low cost, and it is promising for emergency situations and therapy. This work proposes a tri-stage CXR image based COVID-19 classification model using deep learning convolutional neural networks (DLCNN) with an optimal feature selection technique named as enhanced grey-wolf optimizer with genetic algorithm (EGWO-GA), which is denoted as CXGNet. The proposed CXGNet is implemented as multiple classes, such as 4-class, 3-class, and 2-class models based on the diseases. Extensive simulation outcome discloses the superiority of the proposed CXGNet model with enhanced classification accuracy of 94.00% for the 4-class model, 97.05% of accuracy for the 3-class model, and 100% accuracy for the 2-class model as compared to conventional methods.

1. Introduction

COVID-19 is a disease caused by the respiratory ailment known as severe acute respiratory syndrome coronavirus 2 (SARS-CoV-2), a pathogen strain that had spread to more than 200 countries in the previous year. On March 11th, 2020, the World Health Organization (WHO) labelled the outbreak a pandemic. The manifestations of COVID-19 include causing respiratory problems, heart infections, resulting in fatalities, which seriously threaten the health of the entire world. In around December 2019, in the City of Wuhan, located in the People's Republic of China, the pathogen was originally recorded in humans, which expeditiously crossed the continent perimeters due to persistent mobilities among nations. COVID-19 has adversely impacted the world economy. According to research, the COVID-19 virus has a higher affinity for the lung, which severely impairs its function and quickly mutates before the patient is properly diagnosed, resulting in leading medication [1,2]. The situation is set to be more precarious as symptoms mimic the common flu as reported in cases emerging from Southeast and Central Asia. As per the experts [3], the incubation period of the pathogen is roughly 1 week. The infected person can unintentionally transmit the disease as the patient becomes the carrier during the incubation period. The pathogen is highly infective, and the transmission is more rapid than detection [4]. See (Fig. 1).

However, there are some disagreements stated by the general health research community regarding the precise answers to these queries and they are currently under scrutiny. COVID invades the lungs and impairs the tissues of the host. Some subjects may not exhibit symptoms in the early stages, whereas the majority of the population is febrile and exhibits symptoms such as cough. Other manifestations include sore throats, headaches, and body aches. Presently, the disease is rampant due to the scarcity of rapid detection techniques. There were numerous fatalities in 2020 all over the world. The binding affinity of the pathogen to the lungs and respiratory tract is higher, which serves as the medium for the rapid spread of the disease. This process results in inflammation, causing the filling of discharged fluid into the air sacs, which reduces oxygen intake. Doctors and other healthcare providers are facing a significant challenge to the early and accurate detection of the pathogen to decrease the mortality rate. In addition to this, global climate change has

* Corresponding author.
E-mail addresses: anandbabu.gopathoti@gmail.com (A. Gopatoti), vijihicet@gmail.com (P. Vijayalakshmi).

https://doi.org/10.1016/j.bspc.2022.103860
Received 30 January 2022; Received in revised form 17 May 2022; Accepted 4 June 2022
Available online 6 June 2022

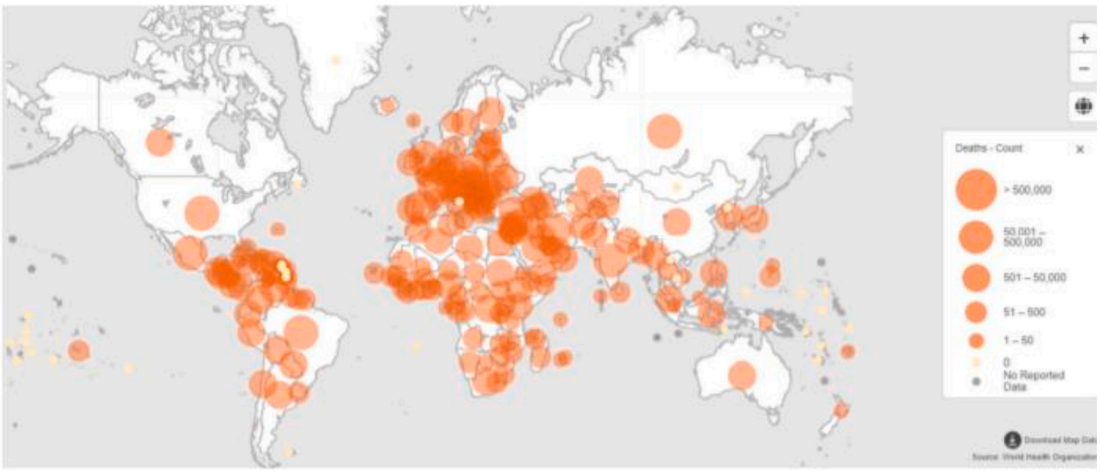

Fig. 1. WHO released a map of COVID-19-related death rate throughout the world (source: WHO).

already had adverse effects in the form of other diseases on the population, and this dual impact is unfathomable. At present, the contagion is escalating globally [5]. The majority of cases were reported in North America, Europe, and Southeast Asia. Globally, over 468 million confirmed cases and over 6 million fatalities have been documented as of March 20, 2022. Further investigations into a potent screening procedure are sacrosanct for diagnosing and quarantining infected patients. Healthcare professionals and researchers are striving to enhance the plan of treatment and the capacity test via the execution of multifunctional evaluation to stop the spread of disease and fatalities. Several modalities to detect the virus exist. Some of them are reverse transcriptase-polymerase chain reaction (RT-PCR) test [6], CXR image [7,8], rapid antigen [9], computed tomography (CT) scan [10], and serological test [11], etc.

In the recent past, the most fruitful diagnostic modality was RT-PCR in the detection of pathogens, but it has some restraints such as prolonged duration of detection and a lower detection rate. Scrupulous requirements in labs and multiple elements of the testing contribute to the downsides [12,13]. Scientists have been making decent efforts to overcome these restraints of RT-PCR investigations, i.e., to enhance the detection of pathogens. In October 2020, WHO recommended chest imaging as a profound diagnostic modality based on the accuracy with which it detects clinical symptoms of recovered people post-infection [14]. There are other types of diagnostic tests, which include chest MRI, ultrasound, CXR, CT, and tissue extract of the lung by needle biopsy, which are proving to be efficacious. In this case, CT has a higher sensitivity for early pneumonic alteration, illness development, and alternative diagnosis; intravenous contrast medium was required for pulmonary thromboembolism diagnosis. Further, CT scans are not enough to identify COVID-19 due to loss of features. Thus, this imaging should be used in conjunction with clinical and laboratory tests. In addition, COVID-19 was identified from the peripheral and posterior lungs by performing ground glass opacities (GGO) based bilateral distribution with or without consolidation. However, the CT screening failed to extract the accurate GGO features. Furthermore, both the Italian Society of Radiology (SIRM) and the American College of Radiology (ACR) did not promote CT as a screening tool for COVID-19 detection, instead recommending it only for symptomatic patients with particular clinical criteria. Therefore, CXR is widely suggested by ACR and SIRM to diagnose COVID-19. The viable speed, the economic aspects and the lucidity for the radiologists make CXR a favored tool for emergency cases and treatment.

Currently, CXR is a substantial tool to detect the disease in contrast to CT imaging, which has a tedious process for developing images and, moreover, the scanners are expensive, hence unavailable in underdeveloped countries. Furthermore, pregnant women and children are subjected to hazards like high radiation [15]. Instead, CXR imaging remains a vital aspect in many epidemiological and medical situations due to the wide range of its availability [16,17]. Nevertheless, some irregularities were spotted in the images drawn from the CXR of infected populations, which were elucidated in previous research [18]. Machine learning methodologies [19,20] are exceptionally popular in healthcare applications. In the recent past, image or object recognition and classification tools like CNN, along with deep learning (DL) algorithms, have been utilized in diagnosis, especially of cancers, through image classification. To generate segmentation, two extensive convolutional residual networks were proposed by Li and Shen [21], which were classification results and feature extraction from skin lesions. The refinement of classification results was based on the lesion index calculation unit. A quotient of 0.912 precision was achieved in diagnosing cancer resulting from DL frameworks. Liao et al., [22] proposed a multitask DL methodology to improve diagnostic capabilities for twelve different types of cancer when expression data are insufficient. Nevertheless, the comparison of performance with pre-existing similar works was not done by the authors. A study conducted by Yoo et al., [23] in which prostate cancer was detected in 427 subjects by an automated CNN-based method using an MR imaging technique, namely DWI (diffusion weighted magnetic resonance imaging), The skin cancer categorization was illustrated by Esteva et al., [24], which was based on 129,450 clinical skin lesions and 3374 dermoscopic images via a pretrained Inception V3 CNN model. The images utilising pixels and disease label inputs were the tools which assisted the comprehensive CNN training. Medical imaging, in conjunction with artificial intelligence, has played a significant role. The configuration and deployment of tools associated with AI for image classification of the contagion within a short period of time with limited data could be utilized on an urgent basis to equip the fight against the pandemic. Recently, it was discovered by radiologists that the DL instituted in AI was handy in the detection of tuberculosis by CXRs, which is analogically useful to identify lung aberrations pertaining to COVID-19, which could aid clinicians to determine the disposition of treatment confined to at-risk COVID-19 patients. The contribution of medical imaging as a predominant source of information was confirmed by many proficient, which is now serving as a tool for validating the early diagnosis of the contagium and supplemented integration of AI to chest imaging can assist in delineating the complications of COVID-19. The predominantly adapted imaging technique by hospitals to diagnose COVID-19 infection is the CXR modality, specifically in Spain as the first image-based perspective. The protocol specifies that if a clinical conjecture with regard to infections occurs after the physical exam of a subject, a specimen of nasopharyngeal exudate is drawn for conducting RT-PCR accompanied by the imaging of CXR film. The PCR interpretation is a tedious process which takes

several hours. Therefore, for an expedited clinical assessment, the data revealed from the CXR mimics a predominant role. This leads to the two conclusions that the patient could be sent home while the results of the etiological analysis could be awaited, which is based on the normal readings of CXR and a stable clinical condition. In the event that the CXR film exhibits disease findings, the subject will be hospitalized for close observation. By and large, the abnormal or normal findings on the CXR determine the clinical decision whether to discharge the patient or to retain the patient in the hospital for further evaluation. Furthermore, given the recent increase in new COVID-19 cases and the resumption of everyday activities throughout the world, the need to contain the pandemic should be underlined even more. In medical analysis, it is constantly vital to improve effectiveness in illness diagnostic performance; even a small increase in accuracy may have a significant impact. In order to achieve improved accuracy, optimum feature selection approaches such as heuristics and metaheuristics are commonly used for feature extraction and selection. Evolutionary computation techniques have recently gained a lot of consideration as a vital metaheuristic family member. Moreover, several feature extraction and selection algorithms were used in medical diagnosis applications [25–27]. As a result, the goal of this paper is to build an efficient feature selection approach called EGWO-GA that is combined with deep CNN for improved diagnosis of CXR images. The novel contribution of this work is as follows:

- Introducing a tri-stage CXR image-based COVID-19 classification model using DLCNN with an optimal feature selection technique named EGWO-GA.
- Implementation of the 4-class CXGNet model for classifying the normal, Pneumonia viral, Pneumonia bacterial, and COVID-19 classes. In addition, the implementation of the three-class CXGNet model for classifying the normal, Pneumonia, and COVID-19 classes. In addition, the implementation of the 2-class CXGNet model for classifying the COVID-19 and normal classes
- The CXR dataset is regrouped based on 4-class, 3-class, and 2-class models, and all CXGNet models are trained with these individual datasets.
- Performance evaluation shows the proposed CXGNet model resulted in superior performance as compared to the existing classification methods for all models and diseases.

The rest of the article is as follows: Section 2 describes the related work of CXR image classification done so far. Section 3 explains the proposed methodology. Section 4 deals with the simulation results and discussion of existing and proposed classification models for CXR imaging. Section 5 concludes the proposed work with possible future directions followed by references.

2. Related work

In the recent past, the virus was subjected to a nomenclature of COVID-19 by the WHO, which had been spreading intrusively in several countries around the globe. Primary manifestation of the disease is analogous to that of the pneumonia classes, which is distinguished by molecular assays like genetic testing and imaging investigations, i.e., CT, CXR etc. Accelerated pathogen detection contributes to disease containment. Further, CXR and CT Chest are the radiology methodologies that play a pivotal role in diagnosing the disease. The perspective of diagnostic systems pertaining to imaging is widely varied, ranging from the process of feature generation to representation learning. The DLCNN is a prominent and effective approach for diagnosing COVID-19 from archived images. Numerous assessments have been conducted to weight the recent contributions to the detection of COVID-19 contagion [28–30]. For instance, a CNN was implemented, which was hinged on a module referred to as the Inception network [31]. CT images were assorted into 3 categories: bacterial pneumonia, COVID-19 and normal, which are classified by a re-oriented version of the ResNet50 pre-trained network [32]. CNN was used to assemble images of the CXR modality that had been pre-trained to high level attributes [33]. The spotting of COVID-19 cases was made possible by the installation of these attributes into the support vector machine (SVM). Furthermore, four subsets of non-COVID-19, COVID-19, bacterial infection, viral infection, and normal CXR images were administered with a CNN framework called COVID-Net [34]. The assessment [35] functioning of trailblazing CNN architectures recommended previously for medical image classification was based on the CXR image manifestations of normal incidents, pneumonia, and COVID-19 disease. The study in [36] aimed at detection of COVID-19 using CXR imaging using the advantages of DL-based decision tree classifier, where the authors employed three DL-based CNN models for binary decision trees, which classify the CXR images as abnormal or normal. If it is abnormal, then it classifies the tuberculosis or non-tuberculosis and also classifies the abnormality as COVID or non-COVID. Bacellar et al., [37] developed a pretrained set of DL models like Inception, VGG, EfficientNet, and ResNet with continuative to computer vision AI systems. In addition, they have also designed a web application that enables the users or hospitals to upload the CXR scans for the purpose of detecting the COVID-19 presence within them. Sahlol et al., [38] implemented hybrid DL models for COVID-19 classification from CXR datasets by unifying the Inception architecture and the marine predators' algorithm, where the first one is for extracting the features and the latter one is for selecting the optimal features from extracted features. The study addressed [39] the recognition of CXR scans from pneumonia and normal cases induced by other viruses, where an efficient ML classifier has been employed with the usage of global image feature extraction and the attainment of features from both spatial and transform domains, unlike most of the existing ML models. Sen et al., implemented the COVID-19 detection scheme from chest CT images using an approach of bi-modular hybrid module [40], where CNN architecture is employed for the extraction of features and then a bi-stage feature selection model (i.e., a combination of guided feature selection and the dragonfly algorithm) has been utilised for finding the optimal features. Finally, an SVM classifier is used to classify the non-COVID-19 and COVID-19 CT images.

Osman et al., [41] recommended a combined scheme of locality weighted learning with a self-organization map for COVID-19 identification from CXR datasets. Hosny et al., [42] suggested the portable design and development of the COVID-19 diagnosis mechanism using a Raspberry Pi Linux embedded system for the requirements of minimal memory. They have employed both local and global feature extraction techniques such as local binary pattern and multi-channel fractional order Legendre Fourier moments. Recently, a 2-stage CXR classification system using deep-CNN has been developed for detecting the abnormalities and textual feature extraction that can be associated with particular COVID-19 virus signatures [43]. Munuswamy et al., [44] proposed FractalCovNet for lesion region localization by segmenting the CXR images with the integration of U-Net and fractal blocks. Furthermore, the same FractlCovNet is incorporated with a transfer learning approach for the classification of COVID-19 from CXR images. Ozturk et al., [45] proposed the DarkNet, which consists of a you-only-look-once (YOLO) network for object detection. Furthermore, the DarkNet contains 19 layers with convolution and MaxPooling layers. However, this method suffers from high computational complexity. Khan et al., [46] proposed CoroNet, which is developed by DLCNN models with the Xception architecture. However, the CoroNet resulted in reduced accuracy in multi-class classification on the standard COVID-19 dataset [47]. Wang et al., [48] proposed CT scan-based COVID-19 detection using a feedforward neural network (FFNN). Initially, features are extracted from CT images using a wavelet Renyi entropy approach. Then, FFNN was used to perform the classification operation, and a three-segment biogeography-based optimization approach was also developed to reduce the losses generated in the network. Yu-Dong Zhang et al., [49] developed the 5-layer DLCNN model with two fully connected blocks

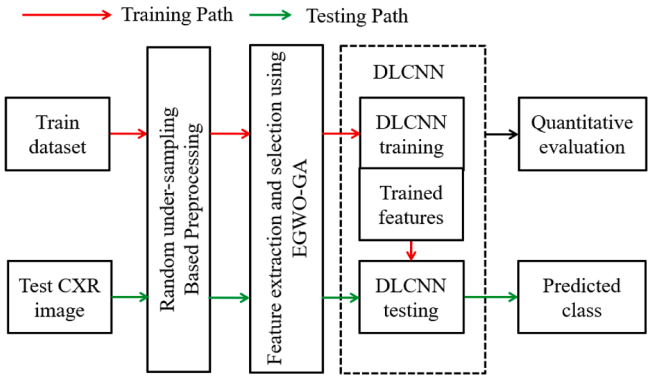

Fig. 2. Proposed CXGNet model block diagram for CXR image classification.

and three convolution blocks. However, this method considers the dataset with a smaller number of images, which means it cannot be useful in practical scenarios. Wang et al., [50] developed a 12-layer deep fractional max pooling neural network. However, all these conventional models were not considered for optimal feature extraction with multi-class classification methods, which resulted in reduced classification performance.

On reviewing the analysis, the evidence suggests that in spite of the achievements of DL in the detection of COVID-19 from CT and CXR images, the precision of ML and DL models is affected by data impurities (e.g., overlapping classes). Moreover, the classification system performance of the above literature can be further enhanced by consolidating an optimal feature selection algorithm with improved classification precision.

3. Problem statement

The best method for detecting COVID-19 is RT-PCR. This manual process is laborious, and the requirement for specialized kits is an important factor which is prone to deficiency in inaccessible areas of a country due to socio-economical and geological barriers. Instead, the rapid antigen test detects antigens of the pathogen in specimens drawn by a nasal swab, but this procedure is subjected to higher incidences of false negatives. The serological test functions by detecting the antibodies produced by the immune system in response to parasites in the blood sample extracted from the patient. Nevertheless, the investigation only detects the IgG and IgM antibodies, which are produced after and during recovery, and so do play a key role in early detection. The CXR and CT scan utilize the spectrum of electro-magnetic ranges which are invisible for the detection of an anomaly, which adds to preliminary detection and provides high clinical relevance. In view of this proposal, we will discover the new computer-aided diagnosis for CXR tests that are economical, and the results are relatively comprehensible. The CXR tests are handy, consisting of a compact version with an unknown risk of radiation. Contrastingly, patients under CT imaging are more prone to the risk of radiation, they are expensive, require expertise for handling, and are non-portable, which in conclusion provides a conjecture that CXR is more preferable than CT scans.

4. Proposed methodology

The proposed CXGNet model uses CXR images as input to detect COVID-19. The test images are first preprocessed, with undesirable parts removed to identify the region of interest (ROI). The proposed CXGNet model can detect pneumonia diseases as well. The proposed CXGNet model also takes into account the EGWO-GA based feature extraction and feature selection approach. This technique is capable of extracting a sufficient number of retrieved characteristics to reliably identify COVID-19. The best characteristics are then combined and sent into the DLCNN classification model as input. The testing and training phases of the proposed CXGNet design are depicted in Fig. 2, which is also represented by an algorithm in Table 1. The dataset contains different types of CXR images, including low-quality, speckle-affected, and high-quality images. These strategies might be used to successfully overcome input image quality restrictions. Following that, EGWO-GA was utilized to extract disease-specific features from the CXR images. Finally, the DLCNN classifies the different types of diseases presented in the CXR images. Further, the proposed work is implemented as a tri-phase model such as 4-class, 3-class, and 2-class CXGNet models to classify the multiple diseases. To perform the simulations, these three models are individually trained and tested using three diverse dataset combinations.

Table 1
Proposed CXGNet model for CXR image classification.

Input: Train dataset, Test image **Output**: Predicted class, Quantitative Evaluation
Step 1: Perform the DLCNN training procedure and develop the trained features from the train dataset. **Step 2:** Apply test CXR image to random under sampling-based preprocessing, so noises, size mismatches presented in the dataset will be removed. **Step 3:** Apply EGWO-GA *meta*-heuristic optimization on the pre-processed outcome for extracting the features and selecting the optimal features. **Step 4:** Perform the DLCNN testing procedure, which compares the test features with pre-trained dataset features. **Step 5:** The DLCNN model classifies the predicted class of test image and then perform the quantitative evaluation for measuring the various metrics.

4.1. Image preprocessing

Image preprocessing is a key step in the classification process, which is used to remove the noise and enhance the low quality CXR images. This work utilised the random undersampling based preprocessing method and extracted the ROI of CXR images. The ROI is used to remove unnecessary text and machine annotations from surrounding CXR images. The ROI was established by concentrating on the lung region area, which is used to acquire useful information in the focused area. A rectangle box is used for focus, and the rectangle is then used to produce a mask. The region outside the ROI was assigned as zero using logical indexing, and the region inside the ROI is enhanced. In order to maintain precise data while decreasing distortion and noise in the CXR, random under-sampling was recommended for this effort. While resampling any noise in a CXR, resampling algorithms preserve important information. Information-preserving resampling algorithms are best for extracting significant features from noisy CXR images. Using speckle-affected images, they were used to evaluate resampling performance throughout the testing phase. Edge information may be preserved and enhanced while noise is reduced via anisotropic diffusion resampling. The edge information, as well as noise, is detected by the gradient operator. For strong speckle and low contrast CXRs, this approach detects noise gradient changes that may extend beyond the edge gradient. These changes destroy more of the edge information than the noise, which makes resampling less accurate.

4.2. Feature extractor

Features Extraction plays a significant research area in computer science based on image processing with medical image diagnostic applications. The extraction and selection of subset characteristics of features is a tough task. As the size of features increases, the computational complexity of the network also increases. Features are not the lower dimension of input images. The features are the statical attributes in the vector format. Sometimes, features can be solitary values, which hold the pixel information. Feature extraction and selection is a *meta*-heuristic application that selects the most relevant and informative features while avoiding noisy and redundant characteristics. When the search

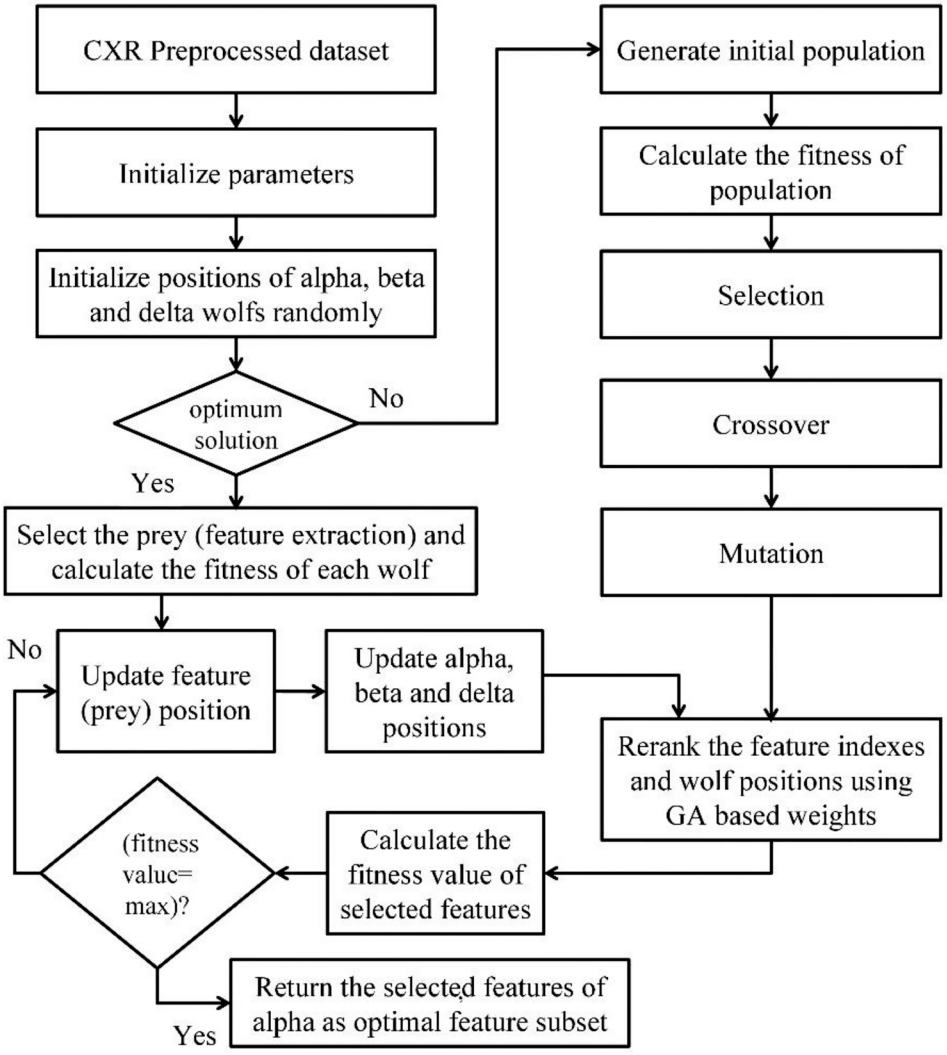

Fig. 3. Flowchart of EGWO-GA feature extraction and optimal feature selection.

space gets excessively large, feature selection becomes a difficult and complicated challenge. Recently, bio-optimization approaches have been introduced for reducing the complexity of systems by extracting the best features. The flowchart of the EGWO-GA flowchart for extracting features and selecting optimal features is shown in Fig. 3.

The EGWO-GA algorithm is a bio-inspired metaheuristic, which was developed by understanding the hunting mechanisms, leadership hierarchy, and social behavior of grey wolves. Generally, the wolves live as a group in their social behavior, and each group contains a multiple of four levels of wolf population. In this group, alpha (α) wolves are the most dominant members. Then beta (β) and delta (δ) wolves are the middle dominant members, and finally omega wolves are the least dominant members. These wolves function together, and under beta wolf leadership, they will start the hunting mechanism. The mathematical model of an EGWO-GA has three stages: encircling, hunting, and attacking the prey.

4.2.1. Encircling prey

Encircling prey is the initial step of the hunting of wolves. The grey wolf will change its position automatically based on the prey position in the search space. To describe the operation of encircling mathematically, three coefficients are derived as follows:

$$\overrightarrow{D_\alpha} = |\overrightarrow{C_1}.\overrightarrow{X_\alpha(t)} - \overrightarrow{X(t)}|, \overrightarrow{D_\beta} = |\overrightarrow{C_2}.\overrightarrow{X_\beta(t)} - \overrightarrow{X(t)}|, \overrightarrow{D_\delta} = |\overrightarrow{C_3}.\overrightarrow{X_\delta(t)} - \overrightarrow{X(t)}| \quad (1)$$

Here, the position vector of grey wolf is indicated by the $\overrightarrow{X(t)}$ with $\overrightarrow{A}$, $\overrightarrow{C}$ and $\overrightarrow{D}$ as its coefficient vector with respect to each current iteration (t). Then, the alpha position vectors is indicated by $\overrightarrow{X_1}$, beta $\overrightarrow{X_2}$ and delta position vectors is indicated by $\overrightarrow{X_3}$. They are calculated as follows:

$$\overrightarrow{X_1} = \overrightarrow{X_\alpha} - \overrightarrow{A_1}.\overrightarrow{D_\alpha}, \overrightarrow{X_2} = \overrightarrow{X_\beta} - \overrightarrow{A_1}.\overrightarrow{D_\beta}, \overrightarrow{X_3} = \overrightarrow{X_\delta} - \overrightarrow{A_1}.\overrightarrow{D_\delta} \quad (2)$$

$$\overrightarrow{X(t)} = \frac{\overrightarrow{X_1} + \overrightarrow{X_2} + \overrightarrow{X_3}}{3} \quad (3)$$

From the above equation, it is observed that the position vectors play a crucial role in the feature selection procedure. If the dominant wolves reach near to the grey wolves, then the grey wolves will run away from their original position based on the average weights of delta, beta, and alpha. Here, the best features are selected by the alpha wolves as it's nearer to prey in social hierarchy. Then, the alpha wolf is treated as the leader. The beta and delta wolves contain the lowest probability of features. Hence, in Eq. (3), alpha positions are dominant as their weights are much larger than the other wolves' weights, respectively.

The hunting and searching processes are performed by the alpha wolves, whereas monitoring operations are performed by the beta wolves, and finally the less important role is played by the delta wolves, respectively. The dominant grey wolves surround the prey in the social hierarchy manner. It means the alpha is number one in position as it is

nearest to the grey wolves, then the beta is ranked as the second position as it is nearer to the pack after the alpha. And finally, delta is ranked in third place.

All wolves have the power to shift their position and leadership levels depending on the location of the prey. The omega wolves are handled as position-movable wolves in this process. This phenomenon can be utilized for the purpose of best feature selection with multi-objective optimization. To implement this, fitness functions are developed by using the minimum or maximum position update. During the searching procedure, the temporary prey is selected, and COVID-19 features are selected. But, during the hunting procedure, accurate prey is selected, and based on the prey, accurate COVID-19 features are selected properly. As the locations of the omega wolves change, the positions evaluated in Eq. (3) must be changed on a regular basis based on the new weights. The GA is added to the EGWO algorithm for this weight update process. The following is a description of the procedure:

- When the hunt begins, the wolf closest to the prey is treated as the alpha, and the other wolves are ignored. The alpha wolf changes its position and starts looking for new prey based on what it sees.
- If the features are retrieved, the alpha weight is set to 1.0 at the start of the search, and the weights of other wolves are set to zero at the same time. These initialization weights can change themselves based on where the prey is and what features are available.
- During the final state, the delta, beta, and alpha have equal weight and encircle the prey based on perfect features. All the wolves start the prey-based feature searching operation from the beginning to the end with automatic wolf rank updation.
- It means beta replaces the position of alpha and delta replaces the position of beta, and finally the original alpha finds the features respectively based on the cumulative iteration number (*iter*). As per this principle, as the original alpha receives identifies the prey, then its weight is reduced and beta and delta wolves' weights are increased respectively. Thus, all of the weights are summed up and the result is the outcome as 1.

Thus, Eq. (3) is changed according to the perception of GA. The above-mentioned hypothesis is mathematically formulated as follows:

$$\overrightarrow{X(t+1)} = w_1 \overrightarrow{X_1} + w_2 \overrightarrow{X_2} + w_3 \overrightarrow{X_3} \tag{4}$$

$$w_1 + w_2 + w_3 = 1 \tag{5}$$

Here, w_1, w_2 and w_3 indicates the weights of alpha, beta and delta, which are optimized by using GA.

4.2.2. GA based crossover and mutation

The crossover operation integrates information from several solutions to produce a new offspring, which is a process of producing novel solutions from the already presented population. The crossover procedure broadens the population's variety and improves exploitation potential. For a number with N bits, a single point crossover, $cp_i, i = 0 to N-1$ is chosen at random. Further, the offspring of the three recommended solutions ($\vec{w}_1$, $\vec{w}_2$, and $\vec{w}_3$) of weights and feature indexes comprises of the first solution's pre-cp_i part followed by the second solution's post-cpi segment. The crossover process is represented by the equation below.

$$\begin{aligned} offspring = [&\overrightarrow{w_1}(section < cp_i) + \overrightarrow{w_2}(cp_i > section), \overrightarrow{w_2}(section \\ &< cp_i) + \overrightarrow{w_3}(cp_i > section), \overrightarrow{w_3}(section < cp_i) + \overrightarrow{w_1}(cp_i \\ &> section)] \end{aligned} \tag{6}$$

The mutation operator makes a random alteration to one or more components of the offspring. This is used to keep the convergence from happening too soon. The mutation process is used to improve the position of a particular solution around a set of randomly chosen leaders. The coordinates are then updated using a random point $mp_i, i = 0 to N-1$ as the offspring number with N bits, which is picked at random. The mutation process is represented by the equation below.

$$\vec{\gamma}_1, \vec{\gamma}_2, \vec{\gamma}_3 = Mutation(offspring) \tag{7}$$

Here, $\vec{\gamma}_1, \vec{\gamma}_2, \vec{\gamma}_3$ represents the crossover and mutation processes and reflect the revised location. To conclude, this part presents two alternative changes to the original GWO. The initial adjustment pushes the parameter a to vary exponentially, hence increasing the number of exploration iterations. The second change is to apply the crossover and mutation processes to the $\vec{G}_1$, $\vec{G}_2$, and $\vec{G}_3$ solutions to get the revised positions of $\vec{\gamma}_1, \vec{\gamma}_2, \vec{\gamma}_3$. The exploration process is aided by the crossover operator, whereas the exploitation step is aided by the mutation operator. The proposed EGWO-GA offers greater exploration and exploration capabilities than the original GWO, because of combining these enhancements. These weights satisfy the weight updation rule $\vec{\gamma}_1 > \vec{\gamma}_2 > \vec{\gamma}_3$. Even though, alpha having highest priority, its weight decreased from 1 to 0.33 during the searching procedure. Similarly, at the same time the weights of the delta and beta raised from 0 to 0.33 respectively.

For this purpose, cosine function is used with an angle θ to be varied in the range of [0, cos (1/3)] on the weight $\overrightarrow{\gamma_1}$; and all the weights are changed with the cumulative iteration number. If *iteration* = 0, then $\overrightarrow{\gamma_2} \cdot \overrightarrow{\gamma_3} \to 0$ and similarly If *iteration* = ∞, then $\overrightarrow{\gamma_1}, \overrightarrow{\gamma_2}, \overrightarrow{\gamma_3} \to 1/3$ respectively. Thus, this work introduced the arc-tangent function on *iteration* and results the outcome as angular parameter φ.

$$\varphi = \frac{1}{2}\arctan(iteration) \tag{8}$$

Here, *it* varied from 0 to $\pi/2$. Mathematically $cos\left(\frac{\pi}{4}\right) = sin\left(\frac{\pi}{4}\right) = \frac{\sqrt{2}}{2}$; if w_2 increased from 0 to 0.33 along with *iteration*, then the above-mentioned condition. The angular parameter majorly depending on *iteration* and if *iteration* $\to \infty$, then $\theta \to arccos(1/3)$, $cos\,\varphi$ and $sin\,\theta$.

$$\theta = \frac{2}{\pi}.arccos\frac{1}{3}.\frac{2}{\pi} \tag{9}$$

if *iteration* $\to \infty, \theta \to arccos(1/3), = 1/3$, Then the weight coefficient w_2 will be calculated easily. Thus, the new positions by using the new weight coefficients are calculated as follows.

$$w_{1^*} = \cos\theta \tag{10}$$

$$w_{2^*} = \frac{1}{2}\sin\theta\cos\varphi \tag{11}$$

$$w_{3^*} = 1 - w_1 - w_2 \tag{12}$$

The omega wolves are changed their position based on the directions of $\overrightarrow{A}$ and controlling parameter *a*.

- if $\overrightarrow{A} > 1$, then the grey wolves changed its positions or run-away from dominants. At the same time, an omega wolf also changed its positions from the prey and creates the more searching space for other wolves. This phenomenon is treated as the global feature search in optimization.
- if $\overrightarrow{A} < 1$, Then the grey wolves changed its positions much nearer to the dominants and finally reaches the prey. This phenomenon is treated as the local feature search in optimization.

The random numbers $\overrightarrow{r_1}$ and $\overrightarrow{r_2}$ are used to indicate the direction of wolves and they are controlled by controlling parameter α and results in the coefficient vectors as follows.

$$\overrightarrow{A} = 2\alpha\overrightarrow{r_1} - \alpha \tag{13}$$

$$\overrightarrow{C} = 2\overrightarrow{r_2} \tag{14}$$

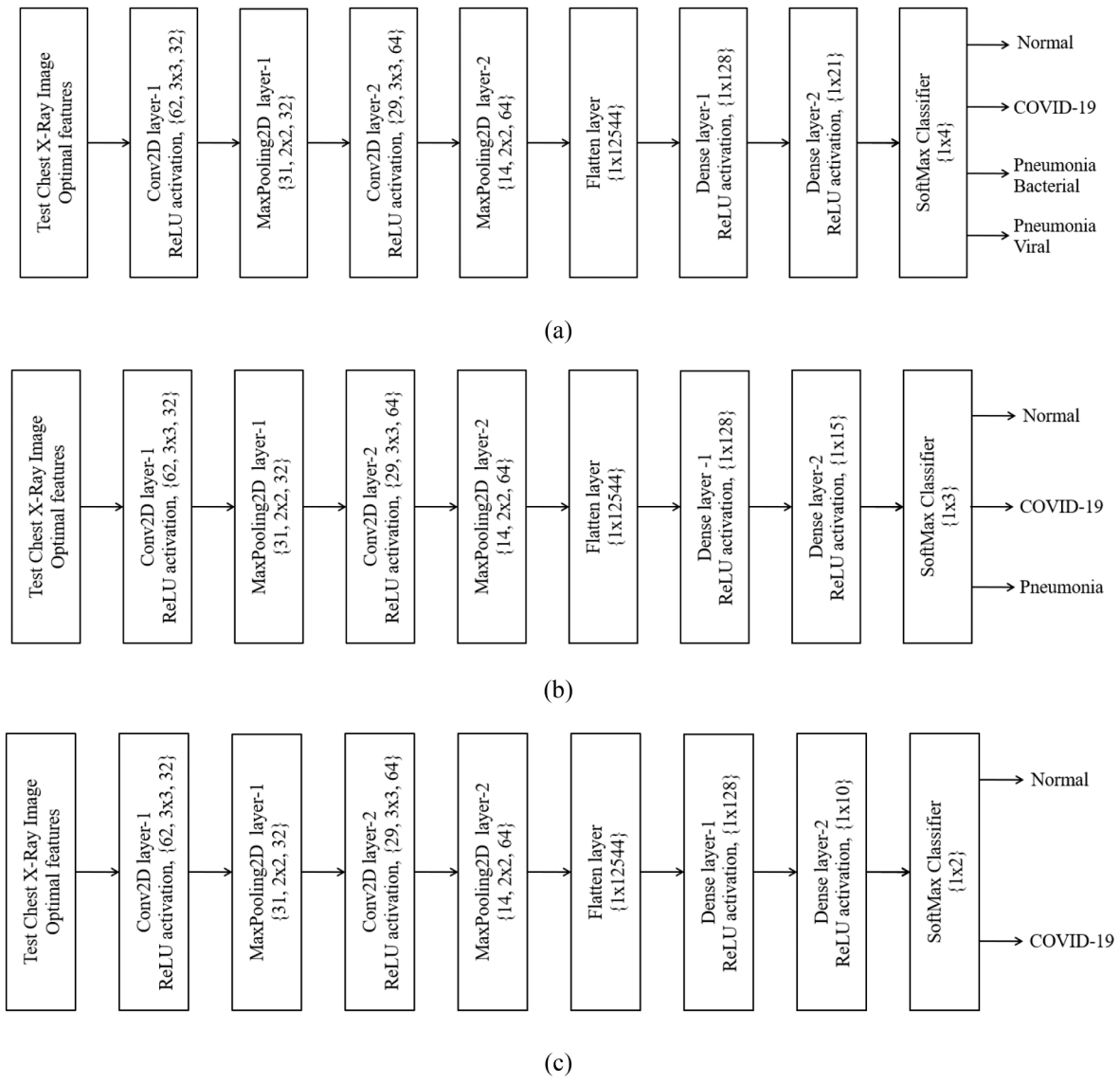

Fig. 4. Multiple prediction models of CXGNet. (a) 4-class CXGNet model. (b) 3-class CXGNet model. (c) 2-class CXGNet model.

From a maximum value of 2, the regulating parameter (a) an is reduced linearly to zero. And it can be calculated by using *iteration* as follows:

$$a = 2(1 - \frac{iteration}{N}) \tag{15}$$

Here, N is maximum iteration number of *iteration* and N is initialized by the users. Finally, the DLCNN architecture requires the greatest and most optimum features in order to increase classification accuracy. The fitness function is employed in this proposal to create the optimal feature selection operation while also increasing classification efficiency.

$$Fitness = aP + (1 - a)\frac{NN - L}{L} \tag{16}$$

Here, *NN* is the total number of features available in the whole dataset, L denotes the length of the extracted, selected feature, and P denotes classification accuracy.

Table 2
Layer wise analysis of CXGNet.

Class	Layer name	Layer dimension	Filter size	No. of filters	Parameters
Same for all classes	Conv2D-1	62x62	3x3	32	896
	MaxPooling2D-1	31x31	2x2	32	0
	Conv2D-2	29x29	3x3	64	18,496
	MaxPooling2D-2	14x14	2x2	64	0
	Flatten	1x12544	–	–	0
	Dense-1	1x128	–	–	1,605,760
Class-4	Dense-2	1x21	–	–	2709
	SoftMax	1x4	–	–	0
Class-3	Dense-2	1x15	–	–	2547
	SoftMax	1x3	–	–	0
Class-2	Dense-2	1x10	–	–	2394
	SoftMax	1x2	–	–	0

4.3. Classification

Many constraints-related optimization problems and classification problems occurring in computer vision applications are solved by using DL mechanisms. The DLCNN is one of the best solutions for the classification process, which extracts the local features from higher inputs and combines them into more complicated features at lower levels. The

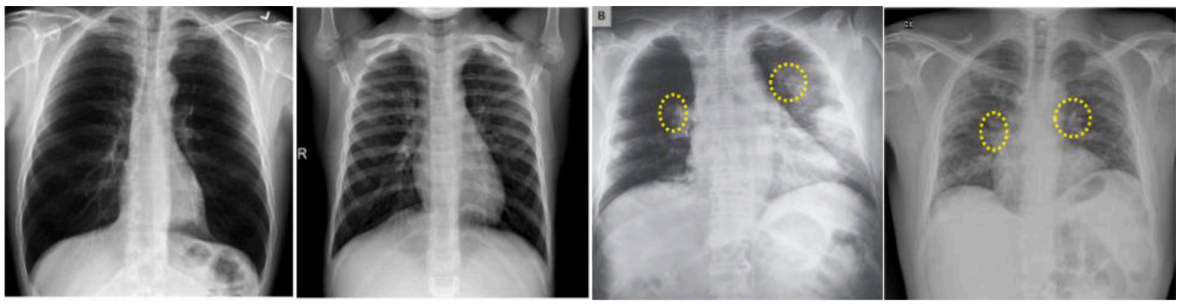

(a) (b) (c) (d)

Fig. 5. Sample dataset (a), (b) normal; (c), (d) COVID-19.

performance of the DLCNN is also improved by updating the weights and kernel sizes with the local connections. Fig. 4 presents the multiple prediction models of DLCNN-based CXGNet, which includes the 4-class CXGNet, 3-class CXGNet, and 2-class CXGNet models, respectively. Table 2 presents the detailed analysis of each layer with layer-wise dimension, filter size or kernel size, number of filters, and parameters, respectively. Stacked ensemble learning is used to stack the CXGNet architecture for performing multi-class classification, which improves the results obtained using a single model. All the layers are combined together and perform the classification operation as follows:

4.3.1. Convolutional layer

The convolution layer is a major operational block in DLCNN, which is used to perform the convolution operation between CXR and the weight matrix and generate the local features. Here, the weight matrix properties depend on the kernel size and activation function. The basic relationship between all the pixels of the CXR image is extracted by using this layer. The mathematical operation of convolution layer is given as follows:

$$F(i,j) = (I^{*}K)(i,j) = \sum_{m}^{M}\sum_{n}^{N} I(i+m, j+n)K(m,n) \tag{17}$$

In this case, the input image or matrix is denoted by, the 2D filter is denoted by with as the filter size, and the 2D feature map output is denoted by F. convolution operation is performed between I, K and generates the F. The resultant output of the convolution layer is applied to the Rectified Linear Unit (ReLU) based activation function, which introduces the non-linearity relationship between various features. The ReLU considers the threshold value as zero and compares the threshold value with the input. If the input feature is less than zero, which results in the output being zero, else the output is input. The mathematical analysis of the ReLU activation function is indicated as follows:

$$f(x) = \max(0, x) \tag{18}$$

4.3.2. MaxPooling layer

The MaxPooling layer in the DLCNN environment is used for down-sampling purposes, which is used to reduce the input spatial size and also reduce the network parameters by factor two. The AvgPool and L2-Norm pooling layers were losing the feature characteristics, whereas the MaxPooling layer extracts the data by searching the input feature range maximum and selecting the best feature properties.

4.3.3. Flatten layer

A flatten layer is used to convert the input pooled three-dimensional feature map into a column-wise feature map. This architecture contains many pooling layers with many pooled feature maps, which are packed into a series. So, this layer puts them into one long column sequentially, one after the other. This layer is primarily used to consolidate all CXR features into a single vector.

4.3.4. Dense layer

The dense layer is an output layer, which is used to generate all possible interconnections between the previous layer neurons and the next layer neurons. So, all the neurons participate in the process of classification. The matrix vector multiplication operation is performed between the preceding layer neurons' row vector and the column vector neurons of the next layer.

4.3.5. Classification process-SoftMax classifier

All the layers presented in the proposed CXGNet architecture are stacked up to make a multi-class DLCNN model. The proposed DLCNN model includes a SoftMax classifier to reduce the complexity by minimizing the training time, which also classifies the COVID-19 classification from CXR. This work increases the filter sizes gradually during the training process. To perform the classification operation, the classifier consists of a bias vector, weight matrix, and activation function. The mathematical relationship between these properties is defined as follows::

$$Output = ReLU(dot(input, kernel) + bias) \tag{19}$$

This holds the different classified classes of COVID-19. Usually, the bias levels and activation function ranges were different for 4-class, 3-class CXGNet models, and 2-class CXGNet models and predicted the classes based on these bias levels. The four-class CXGNet model contains four bias levels, which act as threshold regions and classify the COVID-19, Normal, Pneumonia Bacterial, and Pneumonia Viral classes. Similarly, the 3-class CXGNet model contains three bias levels, which act as threshold regions and classify the COVID-19, Normal, and Pneumonia classes. Finally, the 2-class CXGNet model contains two bias levels, which act as threshold regions and classify the COVID-19 and normal classes.

5. Results and discussion

This work conducted a series of experiments in order to evaluate the performance of proposed approach compared to the state of art approaches. The performance of proposed method evaluated class wise and compared with the conventional approaches for each disease, respectively.

5.1. Dataset description

Datasets play a major role in DL methods. The CXR images are collected from two distinct publicly available image databases to generate a new dataset [47]. A few COVID-19 CXR samples were collected from the Radiological Society of North America (RSNA), which is a legitimate source. Further, Pneumonia viral and bacterial-based CXR images are collected from Kaggle's "CXR Images (Pneumonia)" collection. The simulations are run on 69 COVID-19 images, 73 Pneumonia bacterial images, 81 Pneumonia viral images, and 25 normal images.

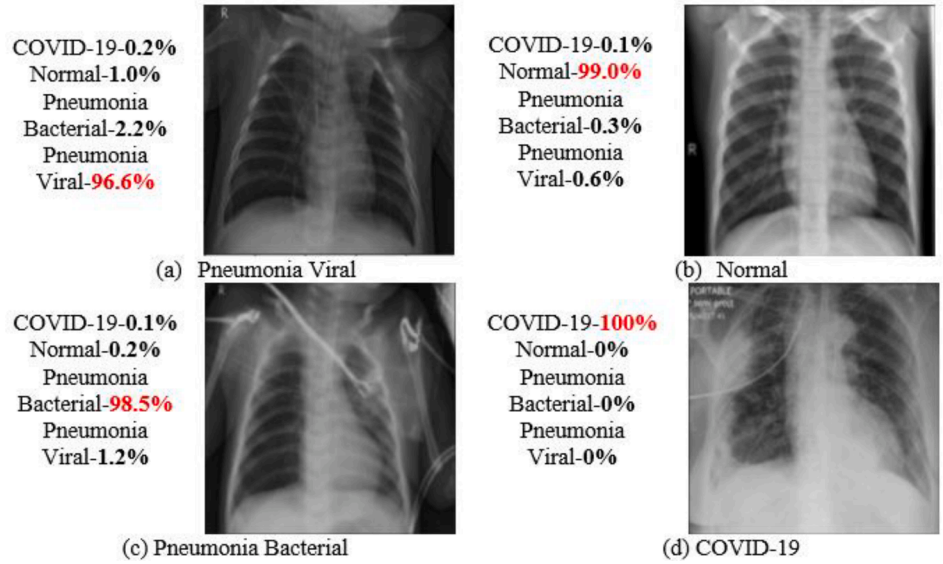

Fig. 6. Few CXR images evaluated by proposed CXGNet method.

Table 3
Overall performance comparison of 4-class, 3-class, and 2-class CXGNet.

Class	Recall (%)	Precision (%)	F-measure (%)	Specificity (%)	Accuracy (%)
2-class CXGNet	100	100	100	100	100
3-Class CXGNet	96.96	94.44	95.38	91.41	97.05
4-Class CXGNet	92.60	95.31	93.74	94.27	94.00

The repeated random subsampling validation method is used to split the dataset into 80% for testing and 20% for testing. The dataset is randomly divided into training and validation in repeated random subsampling validation, commonly known as Monte Carlo cross-validation. Unlikely k-fold cross-validation distributes the dataset into random splits rather than groups or folds.

5.2. Subjective performance evaluation

A comparison of normal and COVID-19 CXR images is shown in Fig. 5. The humidity in the lungs is increased due to COVID-19, so the CXR based COVID-19 images have more whiteness as compared to the normal CXR images. Usually, the radiologists confirm the COVID-19 disease by monitoring these CXR images through the ground glass opacity mechanism. But there is a problem with this method. The COVID-19 based CXR scans look similar to the pneumonia disease images, which can lead to misprediction, misclassification, and improper condition analysis. Thus, this work adopted a DL mechanism to overcome these problems by using computer-aided methods.

From Fig. 6, it is observed that the proposed CXGNet approach accurately predicts and classifies the COVID-19, pneumonia viral, and pneumonia bacterial diseases. In Fig. 6, the highest percentage in red indicates the predicted class. So, the predicted class has much higher values as compared to the undetected classes, which indicates the proposed CXGNet method extracts the accurate disease dependent features and those features are matched to that certain class only.

5.3. Performance comparison

This section gives the performance comparison of proposed CXGNet models such as 4-class, 3-class, and 2-class. In addition, the performance of these models is evaluated for each class of diseases using various metrics. Furthermore, the class-wise and disease-wise performance of the proposed CXGNet approach was also compared with the state-of-the-art approaches using recall, precision, F-measure, specificity, and accuracy-based performance measures. Table 3 compares the performance of the proposed CXGNet with 4-class, 3-class, and 2-class modes. The 3-class CXGNet and 4-class CXGNet models contain other pneumonia-based diseases, which have an impact on the performance of the COVID-19 classification. Thus, it is observed from Table 3, the 2-class CXGNet model resulted in superior performance as compared to

Table 4
Performance comparison of various 4-class models.

Method	Precision (%)	Recall (%)	Specificity (%)	F-measure (%)	Accuracy (%)
SOM-LWL [41]	88.27	89.37	86.94	89.13	87.83
CNN [39]	89.83	90.38	90.28	90.29	88.39
FOMP [38]	90.29	91.49	91.38	90.39	90.49
Covid-net [34]	92.60	92.58	93.00	91.83	91.55
Proposed 4-class model using CXGNet	**95.31**	**92.60**	**94.27**	**93.74**	**94.00**

Table 5
Obtained quality metrics of CXR classification using existing and proposed 3-class models.

Method	Precision (%)	Recall (%)	Specificity (%)	F-measure (%)	Accuracy (%)
Dragonfly algorithm [40]	91.38	89.38	89.84	88.47	90.19
DLH-COVID [37]	92.30	91.94	91.39	89.94	93.29
FractalCovNet [44]	94.05	92.37	93.94	92.38	94.38
Proposed 3-class model using CXGNet	**94.44**	**96.96**	**91.41**	**95.38**	**97.05**

Table 6
Performance comparison among 2-class models.

Method	Precision (%)	Recall (%)	Specificity (%)	F-measure (%)	Accuracy (%)
DCNN [43]	91.02	92.39	93.02	93.92	91.23
ResNet18 [36]	92.30	94.28	94.47	92.94	95.38
DRE-Net [32]	95.89	95.58	95.60	94.38	96.70
2-class CXGNet	**100**	**100**	**100**	**100**	**100**

the 3-class CXGNet and 4-class CXGNet models.

Table 4 compares the performance of the proposed 4-class model with existing 4-class approaches such as SOM-LWL [41], CNN [39], FOMP [38] and Covid-net [34] to evaluate the superiority of the proposed CXGNet method. In Form Table 4, it is observed that the proposed 4-class model using CXGNet resulted in enhanced classification performance with better precision, recall, specificity, F-measure, and accuracy of 95.31%, 92.6%, 94.27%, 93.74%, and 94%, respectively. Similarly, Table 5 lists the obtained quality metrics and compares the performance of the proposed 3-class model using CXGNet with the existing 3-class approaches such as the Dragonfly algorithm [40], DLH-COVID [37] and FractalCovNet [44]. From Form Table 5, it is observed that the proposed 3-class model obtained superior classification performance as compared to the existing 3-class models. Table 6 compares the performance of the proposed 2-class model using CXGNet with state-of-the-art 2-class models such as DCNN [43], ResNet18 [36], and DRE-Net [32], whereas the proposed 2-class model outperforms the existing 2-class models by obtaining 100% precision, recall, F-measure, specificity, and accuracy, respectively.

The comparative methods presented in Table 4, Table 5, and Table 6 are developed with individual 4-class, 3-class, and 2-class models. However, the proposed CXGNet method is employed for all three models. Hence, Table 7 lists the obtained quality metrics that are developed using existing 2-class, 3-class, and 4-class classification models as compared to the proposed CXGNet. From Table 7, it is observed that the performance of the proposed CXGNet method is improved for each class of performance as compared to the conventional DarkNet [45], TL-CNN [35] and CoroNet [46] for all the metrics, respectively.

In addition, the class-wise performance comparison of the proposed 4-class CXGNet is presented in Table 8, where the COVID-19 detection performance is higher as compared to other diseases. Thus, this system is perfectly suitable for classifying COVID-19 from CXR images. The simulations were carried out on the 3-claass dataset using the proposed 3-class CXGNet model. The results are presented in Table 9, which gives the improved detection performance for individual COVID-19, Pneumonia, and Normal classes as compared to the individual classes of 4-class CXGNet.

Further, Table 10 compares the performance of the proposed 4-class

Table 8
Class wise performance comparison of 4-class CXGNet.

Class	Precision (%)	Recall (%)	Specificity (%)	F-measure (%)
COVID-19	100	100	100	100
Normal	100	83.33	83.33	90.90
Pneumonia Bacterial	87.50	93.33	93.75	90.32
Pneumonia Viral	93.75	93.75	100	93.75
Average	95.31	92.60	94.27	93.74

Table 9
Class wise performance comparison of 3-class CXGNet.

Class	Precision (%)	Recall (%)	Specificity (%)	F-measure (%)
COVID-19	100	100	100	100
Normal	83.33	100	83.33	90.90
Pneumonia Bacterial	100	90.90	90.90	95.23
Average	94.44	96.96	91.41	95.38

Table 10
Individual class wise performance comparison of 4-class models.

class	Method	Precision (%)	Recall (%)	Specificity (%)	F-measure (%)
COVID-19	Covid-net [34]	80	95.38	88.8	87.48
	CoroNet [46]	93.17	98.25	95.6	94.58
	CXGNet	**100**	**100**	**100**	**100**
Normal	Covid-net [34]	95.1	73.9	80.17	84.38
	CoroNet [46]	95.25	81.5	82.3	90.89
	CXGNet	**100**	**83.33**	**83.33**	**90.90**
Pneumonia Bacterial	Covid-net [34]	87.1	93.1	90	91.37
	CoroNet [46]	86.85	85.9	86.3	93.74
	CXGNet	**87.50**	**93.33**	**93.75**	**90.32**
Pneumonia Viral	Covid-net [34]	67.0	81.9	73.7	78.78
	CoroNet [46]	84.1	82.1	83.1	85.87
	CXGNet	**93.75**	**93.75**	**100**	**93.75**
Average	Covid-net [34]	67.0	81.9	73.7	78.78
	CoroNet [46]	84.1	82.1	83.1	85.87
	CXGNet	**95.31**	**92.60**	**94.27**	**93.74**

Table 7
Class wise performance comparison of mutual methods for all classes.

Class	Method	Precision (%)	Recall (%)	Specificity (%)	F-measure (%)	Accuracy (%)
4-class	DarkNet [45]	88.38	90.39	90.38	88.28	90.13
	TL-CNN [35]	89.18	91.49	91.39	90.40	91.92
	CoroNet [46]	90.29	92.58	94.38	92.26	92.93
	CXGNet	**95.31**	**92.60**	**94.27**	**93.74**	**94.00**
3-class	DarkNet [45]	88.84	91.39	87.02	90.29	86.37
	TL-CNN [35]	89.46	92.39	92.85	93.38	90.39
	CoroNet [46]	90.38	92.40	93.06	94.69	91.38
	CXGNet	**94.44**	**96.96**	**91.41**	**95.38**	**97.05**
2-class	TL-CNN [35]	87.48	83.88	85.57	86.02	87.90
	DarkNet [45]	96.90	92.48	98.08	95.38	92.38
	CoroNet [46]	97.82	94.37	99.00	96.93	96.47
	CXGNet	**100**	**100**	**100**	**100**	**100**

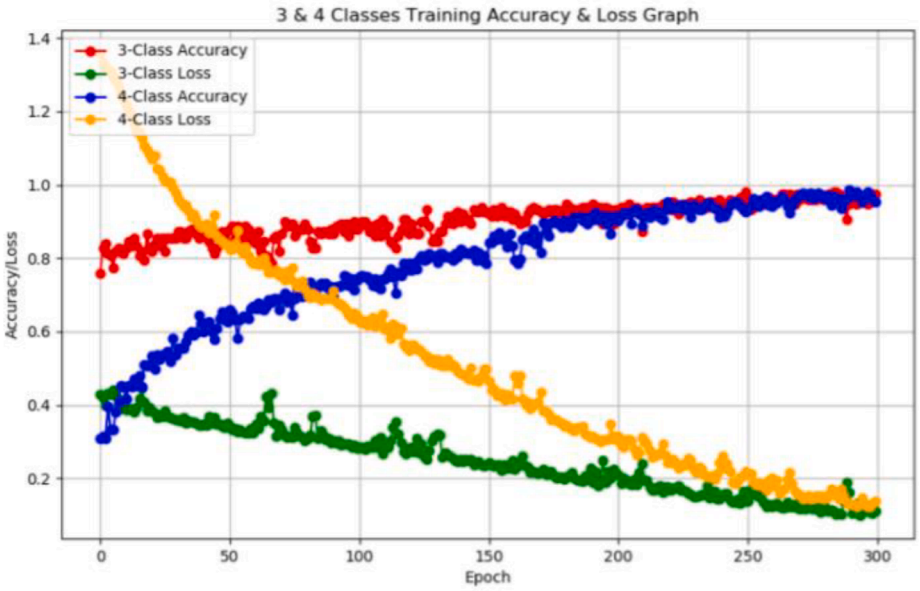

Fig. 7. Performance comparison of accuracy and loss graph for 3-class and 4-class models using proposed CXGNet method.

model with conventional Covid-net [34] and CoroNet [46] approaches. It is also proved that the proposed CXGNet method resulted in superior performance for each class as the EGWO-GA extracts the disease-related features accurately. Fig. 7 presents the training accuracy and training loss performance for multiple values of epoch for both 3-class and 4-class models, respectively. From the graph, it is observed that as the number of epochs is increased, the training accuracy is increased and as the number of epochs is increased, the training loss is decreased, respectively.

6. Conclusion

This article presented a computer-aided detection and classification mechanism for COVID-19 using DL methodology from the CXR images, which classifies the disease quickly as compared to the standard RT-PCR, rapid antigen, and serological tests and reduces the human effort. This work developed three different models, such as 4-class, 3-class, and 2-class CXGNet models. Here, the 4-class CXGNet model is used to classify the normal, COVID-19, Pneumonia viral, and Pneumonia bacterial classes. Then, the 3-class CXGNet model is used to classify the normal, COVID-19, and pneumonia classes. In addition, the 2-class CXGNet model is used to classify normal and COVID-19 diseases. Furthermore, the proposed CXGNet model is developed with random under-sampling-based data preprocessing, EGWO-GA based optimal feature extraction, and selection. The results show that the proposed CXNet obtained superior classification performance as compared to the conventional methods in terms of all performance metrics for three models.

CRediT authorship contribution statement

Anandbabu Gopatoti: Conceptualization, Methodology, Software, Data curation, Writing – original draft, Visualization, Investigation, Writing – review & editing. **P. Vijayalakshmi:** Supervision, Writing – review & editing.

Declaration of Competing Interest

The authors declare that they have no known competing financial interests or personal relationships that could have appeared to influence the work reported in this paper.

References

[1] What does covid-19 do to your lungs? https://www.webmd.com/lung/what-does-covid-do-to-your-lungs#1 (Accessed on 27th September 2021).
[2] P. Galiatsatos, What coronavirus does to the lungs. https://www.hopkinsmedicine.org/health/conditions-and-diseases/coronavirus/what-coronavirus-does-to-the-lungs (Accessed on 27th September 2021).
[3] S.A. Lauer, K.H. Grantz, Q. Bi, F.K. Jones, Q. Zheng, H.R. Meredith, A.S. Azman, N. G. Reich, J. Lessler, The incubation period of coronavirus disease 2019 (COVID-19) from publicly reported confirmed cases: estimation and application, Ann. Internal Med. 172 (9) (2020) 577–582.
[4] M.L. Holshue, C. DeBolt, S. Lindquist, K.H. Lofy, J. Wiesman, H. Bruce, C. Spitters, K. Ericson, S. Wilkerson, A. Tural, et al., First case of 2019 novel coronavirus in the United States, N. Engl. J. Med. 382 (2020) 929–936.
[5] WHO Coronavirus Disease (COVID-19) Dashboard. Available online: WHO Coronavirus (COVID-19) Dashboard | WHO Coronavirus (COVID-19) Dashboard With Vaccination Data (accessed on 27 September 2021).
[6] F. Yicheng, Z. Huangqi, X. Jicheng, L. Minjie, Y. Lingjun, P. Peipei, J. Wenbin, Sensitivity of chest ct for covid-19: comparison to rt-pcr, Radiology (2020), 200432.
[7] M. de Joaquim, R. Lucia, L.V. Placido, C. Milena, A. Laura, C. Eva, N. Jorge, O. Marcos, Deep convolutional approaches for the analysis of covid-19 using chest x-ray images from portable devices, IEEE Access (2020).
[8] L. Wang, Z.Q. Lin, A. Wong, Covid-net: a tailored deep convolutional neural network design for detection of covid-19 cases from chest x-ray images, Sci. Rep. 10 (1) (2020) 19549.
[9] Z. Jinyu, Z. Yichen, H. Xuehai, X. Pengtao, Covid-CT-dataset: a CT scan dataset about covid-19. arXiv preprint, 2020.
[10] M. Nagura-Ikeda, K. Imai, S. Tabata, K. Miyoshi, N. Murahara, T. Mizuno, M. Horiuchi, K. Kato, Y. Imoto, M. Iwata, et al., Clinical evaluation of self-collected saliva by rt-qpcr, direct rt-qpcr, rt-lamp, and a rapid antigen test to diagnose covid-19, J. Clin. Microbiol. (2020).
[11] L.B. Mayara, T. Gamuchirai, K.A. Syed, R.C. Jonathon, H. Louis-Patrick, C.J. James, L. Zhiyi, L. Stephanie, M. Emily, T. Anete, et al., Diagnostic accuracy of serological tests for covid-19: systematic review and meta-analysis, BMJ 370 (2020).
[12] L. Wang, Z.Q. Lin, A. Wong, COVID-Net: a tailored deep convolutional neural network design for detection of COVID-19 cases from chest X-ray images, Sci Rep 10 (1) (2020).
[13] A. Afzal, Molecular diagnostic technologies for COVID-19: Limitations and challenges, J. Adv. Res. 26 (2020) 149–159.
[14] World Health Organization: Use of Chest Imaging in Covid-19. 2020. Available online: https://www.who.int/publications/i/item/use-of-chest-imaging-in-covid-19 (Accessed on 27th September 2021).
[15] H.E. Davies, C.G. Wathen, F.V. Gleeson, The risks of radiation exposure related to diagnostic imaging and how to minimise them, BMJ 342 (feb25 1) (2011) d947–d.
[16] T. Cherian, E.K. Mulholland, J.B. Carlin, H. Ostensen, R. Amin, M.D. Campo, D. Greenberg, R. Lagos, M. Lucero, S.A. Madhi, et al., Standardized interpretation of paediatric chest radiographs for the diagnosis of pneumonia in epidemiological studies, Bull. World Health Organ 83 (2005) 353–359.
[17] T. Franquet, Imaging of pneumonia: trends and algorithms, Eur. Respir. J. 18 (2001) 196–208.
[18] Ng, M.Y.; Lee, E.Y.; Yang, J.; Yang, F.; Li, X.; Wang, H.; Lui, M.; Lo, C.; Leung, B.; Khong, P.; et al. Imaging profile of the covid-19 infection: Radiologic findings and literature review. Radiol. Cardiothorac. Imaging 2020, 2, e200034.

[19] S. Gupta, V. Bharti, A. Kumar, A survey on various machine learning algorithms for disease prediction, Int. J. Recent Technol. Eng. 7 (6c) (2019) 84–87.
[20] R. Nautiyal, P. Dahiya, A. Dahiya, Different approaches of ann for detection of cancer, Int. J. Recent Technol. Eng. 7 (6c) (2019) 88–93.
[21] Y. Li, L. Shen, Skin lesion analysis towards melanoma detection using deep learning network, Sensors 18 (2018) 556.
[22] Q. Liao, Y. Ding, Z.L. Jiang, X. Wang, C. Zhang, Q. Zhang, Multi-task deep convolutional neural network for cancer diagnosis, Neurocomputing 348 (2019) 66–73.
[23] S. Yoo, I. Gujrathi, M.A. Haider, F. Khalvati, Prostate cancer detection using deep convolutional neural networks, Sci. Rep. 9 (2019) 1–10.
[24] A. Esteva, B. Kuprel, R.A. Novoa, J. Ko, S.M. Swetter, H.M. Blau, S. Thrun, Dermatologist-level classification of skin cancer with deep neural networks, Nature 542 (2017) 115–118.
[25] E. Shivhare, V.(. Saxena, Breast cancer diagnosis from mammographic images using optimized feature selection and neural network architecture, Int. J. Imaging Syst. Technol. 31 (1) (2021) 253–269.
[26] R. Mohakud, R. Dash, Designing a grey wolf optimization based hyper-parameter optimized convolutional neural network classifier for skin cancer detection, J. King Saud University- Computer and Information Sciences. (2021), https://doi.org/10.1016/j.jksuci.2021.05.012.
[27] N. Shivsharan, S. Ganorkar, Diabetic retinopathy detection using optimized assisted deep learning model: outlook on improved grey wolf algorithm, Int. J. Image Graphics. (2021), https://doi.org/10.1142/S0219467821500352.
[28] D.i. Dong, Z. Tang, S. Wang, H. Hui, L. Gong, Y. Lu, Z. Xue, H. Liao, F. Chen, F. Yang, R. Jin, K. Wang, Z. Liu, J. Wei, W. Mu, H. Zhang, J. Jiang, J. Tian, H. Li, The role of imaging in the detection and management of covid-19: a review, IEEE Rev. Biomed. Eng. 14 (2021) 16–29.
[29] L. Li, et al., Using artificial intelligence to detect covid-19 and community-acquired pneumonia based on pulmonary CT: evaluation of diagnosis accuracy, Radiology 296 (2) (2020) E65–E71.
[30] F. Shi, J. Wang, J. Shi, Z. Wu, Q. Wang, Z. Tang, K. He, Y. Shi, D. Shen, Review of artificial intelligence techniques in imaging data acquisition, segmentation and diagnosis for covid-19, IEEE Rev. Biomed. Eng. 14 (2021) 4–15.
[31] S. Wang, et al., A deep learning algorithm using CT images to screen for corona virus disease (covid-19), medRxiv 2020.02.14.20023028.
[32] Y. Song, S. Zheng, L. Li, X. Zhang, X. Zhang, Z. Huang, J. Chen, R. Wang, H. Zhao, Y. Chong, J. Shen, Y. Zha, Y. Yang, Deep learning enables accurate diagnosis of novel coronavirus (covid-19) with CT images, IEEE/ACM Transactions on Computational Biology and Bioinformatics, Early Access 18 (6) (2021) 2775–2780.
[33] P. K. Sethy, S. K. Behera. Detection of coronavirus disease (covid-19) based on deep features. Preprints 2020, 2020030300 (doi: 10.20944/preprints202003.0300.v1).
[34] L. Wang, A. Wong, Covid-net: A tailored deep convolutional neural network design for detection of covid-19 cases from chest radiography images, Sci. Rep. 10 (2020) 10549.
[35] I.D. Apostolopoulos, T.A. Mpesiana, Covid-19: Automatic detection from x-ray images utilizing transfer learning with convolutional neural networks, Phys. Eng. Sci. Med. 43 (2) (2020) 635–640.
[36] S.H. Yoo, H. Geng, T.L. Chiu, S.K. Yu, D.C. Cho, J. Heo, M.S. Choi, I.H. Choi, C. Cung Van, N.V. Nhung, B.J. Min, H.o. Lee, Deep learning-based decision-tree classifier for COVID-19 diagnosis from chest x-ray imaging, Front. Med. 7 (2020), https://doi.org/10.3389/fmed.2020.00427.
[37] G. C. Bacellar, M. Chandrappa, R. Kulkarni, S. Dey. COVID-19 chest x-ray image classification using deep learning. medRxiv 2021.07.15.21260605.
[38] A.T. Sahlol, D. Yousri, A.A. Ewees, M.A.A. Al-qaness, R. Damasevicius, M.A. Elaziz, COVID-19 image classification using deep features and fractional-order marine predators algorithm, Sci. Rep. 10 (1) (2020).
[39] A. Zargari Khuzani, M. Heidari, S.A. Shariati, COVID-Classifier: an automated machine learning model to assist in the diagnosis of COVID-19 infection in chest X-ray images, Sci. Rep. 11 (2021) 9887.
[40] S. Sen, S. Saha, S. Chatterjee, S. Mirjalili, R. Sarkar, A bi-stage feature selection approach for COVID-19 prediction using chest CT images, Appl. Intell. 51 (12) (2021) 8985–9000.
[41] A.H. Osman, H.M. Aljahdali, S.M. Altarrazi, A. Ahmed, 2021, SOM-LWL method for identification of COVID-19 on chest X-rays. PLoS ONE 16(2): e0247176.
[42] K.M. Hosny, M.M. Darwish, K. Li, A. Salah, 2021, COVID-19 diagnosis from CT scans and chest X-ray images using low-cost Raspberry Pi. PLoS ONE 16(5): e0250688.
[43] J. Hou, T. Gao, Explainable DCNN based chest X-ray image analysis and classification for COVID-19 pneumonia detection, Sci. Rep. 11 (2021) 16071.
[44] H. Munusamy, J.M. Karthikeyan, G. Shriram, S. Thanga Revathi, S. Aravindkumar, FractalCovNet architecture for covid-19 chest x-ray image classification and ct-scan image segmentation. Biocybernetics and Biomedical, Engineering 41 (3) (2021) 1025–1038.
[45] T. Ozturk, M. Talo, E.A. Yildirim, U.B. Baloglu, O. Yildirim, U. Rajendra Acharya, Automated detection of COVID-19 cases using deep neural networks with X-ray images, Comput. Biol. Med. 121 (2020) 103792.
[46] A.I. Khan, J.L. Shah, M.M. Bhat, CoroNet: A deep neural network for detection and diagnosis of COVID-19 from chest x-ray images, Comput. Methods Programs Biomed. 196 (2020) 105581.
[47] J.P. Cohen, P. Morrison, L. Dao, COVID-19 image data collection 11597 (arXiv: 2003.) 2020. https://github.com/ieee8023/covid-chestxray-dataset.
[48] S.-H. Wang, W.u. Xiaosheng, Z. Yu-Dong, C. Tang, X. Zhang, Diagnosis of COVID-19 by wavelet Renyi entropy and three-segment biogeography-based optimization, Int. J. Comput. Intell. Syst. 13 (1) (2020) 1332.
[49] Y.D. Zhang, S.C. Satapathy, S. Liu, G.R. Li, A five-layer deep convolutional neural network with stochastic pooling for chest CT-based COVID-19 diagnosis, Mach. Vis. Appl. 32 (1) (2021) 1–13.
[50] Wang, Shui-Hua, Suresh Chandra Satapathy, Donovan Anderson, Shi-Xin Chen, and Yu-Dong Zhang. “Deep fractional max pooling neural network for COVID-19 recognition.” Frontiers in Public Health 9 (2021).